Ref.TH.3578-CERN

ψψ PRODUCTION AT COLLIDER ENERGIES

B. Humpert *)

Institut de Physique Nucléaire
Université de Lausanne
CH - 1000 Lausanne, Switzerland

and

P. Méry

Centre de Physique Théorique et
Faculté des Sciences de Luminy
Case 907, F-13288 Marseille Cedex 2,
France

ABSTRACT

We estimate ψψ production at collider energies in the framework of perturbative QCD. The $O(\alpha_s^2)$-$O(\alpha_s^4)$ parton cross-sections, with the non-relativistic approximation for the heavy quark bound states, are used. This first insight into the characteristics of the kinematical distributions allows predictions on the predominance of the quark, gluon or B meson production mechanisms in particular kinematical regions.

---

*) The author acknowledges the kind hospitality of the CERN Theoretical Physics Division, where the essential part of this work was done.

Ref.TH.3578-CERN
April 1983

1. - INTRODUCTION

First results on the reaction $\pi^- p \to \psi\psi + X$ have recently been presented by the NA3 collaboration at CERN[1]. Several theoretical explanations for its production mechanism have been analyzed in the framework of perturbative QCD assuming the non-relativistic approximation[2),3)] for the heavy quark bound states. The main conclusions of these studies are: $\psi\psi$ production at SPS energies is, to a significant fraction, described by the subprocesses $q\bar{q}/gg \to \psi\psi$, although a slight discrepancy with the data persists. The production of $B\bar{B}$ intermediate states with their subsequent decay into ψ's may, however, be ignored.

The clean experimental signature for a final state ψ pair, as well as the simple parton kinematics, which is fully determined as soon as the ψ momenta are fixed, allows an event-by-event study of the constituent dynamics; the ψ may be considered as a probe of the strong interactions. If, at higher energies, heavy (B-) meson production should be significant, the $\psi\psi$ final state will also signal this fact.

Based on the above considerations, we consider it fruitful to carry out an analogous analysis of $\psi\psi$ production at collider energies in order to obtain a cross-section estimate, some hints on the kinematical distributions, and, most of all, on the separability of the different production mechanisms.

In the following, we consider "direct" $\psi\psi$ production by gluon-fusion and $q\bar{q}$ annihilation, and evaluate the characteristics of several B production mechanisms which, at these energies, could very well be of equal importance. The integrated cross-sections expose the relative size, and the rapidity-, transverse momentum-, and $\psi\psi$ mass distributions indicate possibilities how experimental emphasis can be placed on one or the other subprocess.

Our analysis is based on simple models which should become more and more valid as the quark masses grow. We therefore determine the dependence of the cross-sections on the quark masses, thus obtaining predictions for $\psi\psi$ and possibly higher-mass bound states.

In Section 2, we give the parton cross-sections of the considered constituent processes. We expose the angular dependence of the differential cross-sections and point to the fall-off of the integrated cross-sections with increasing subenergy. In Section 3, the integrated hadron cross-sections and the characteristics of the kinematical distributions are presented. In Section 4 we focus on the dependence of the heavy quark masses, and Section 5 closes with the summary.

2. - THE PARTON CROSS-SECTIONS

We introduce the parton subprocesses for $\psi\psi$ production, give formulae for their cross-sections and expose their angular and energy dependence.

Our analysis is carried out in the framework of perturbative QCD, taking graphs of order $O(\alpha_s^2)$-$O(\alpha_s^4)$ into account. The sets of graphs for the different subprocesses, as exposed in Fig. 1, were explicitly verified to satisfy gluon gauge invariance. The "direct" $\psi\psi$ production consists of gluon fusion (Fig. 1a) and $q\bar{q}$ annihilation (Fig. 1b) to produce a (charmed quark) $c\bar{c}$ pair which, via hard gluon exchange, creates another $c\bar{c}$ pair.

A significant fraction of the $\psi\psi$ events has been suggested[4] to originate from $B\bar{B}$ production with subsequent inclusive B $(\equiv b\bar{q})$ meson decay to a ψ. The size of the cross-section for $B\bar{B}$ production and the branching ratio $BR(B \to \psi + X)$ determine the rate. We have analyzed several mechanisms. The most simple B production is given by the lowest order graphs for $gg/q\bar{q} \to b\bar{b}$ (Fig. 1c); B meson formation follows from soft q quark association where the inclusive $b \to B$ transition probability is assumed to be unity.

We also wonder about the cross-section size of exclusive B meson production. We therefore reconsider, in close analogy to "direct" production, the processes of Figs. 1a and 1b where $c\bar{c}$ and associated $q\bar{q}$ production is assumed. We are aware that the use of perturbative QCD is less well justified and that we have limited ourselves to a subclass of graphs. We nevertheless believe that such evaluations will give useful order of magnitude estimates[5].

In our earlier analysis[3], we noticed that $(b\bar{q})$ recombination is likely to be an important mechanism for exclusive B meson production. We therefore also analyze the importance of the "double recombination" process $q\bar{q} \to B_r\bar{B}_r \to \psi\psi$, as shown in Fig. 1d.

The production of an exclusive B meson via (single) $b\bar{q}$ recombination, as suggested in Ref. 2a), is shown in Fig. 1e. Subsequently, recombination between the b quark and the (fast) valence quark $\bar{q}$ of the projectile hadron takes place. The remaining $\bar{b}$ quark associates with a soft q quark. The dynamical distributions of this model were shown to be compatible with the data[2a]; in particular, a leading B meson and a slower $\bar{B}$ meson are expected.

In our investigation, we are also concerned with the size of the background as compared to the actual process under study, inclusive $\psi\psi$ production, which is traced by the leptonic ψ decay modes. We will therefore also evaluate the parton cross-section of the constituent process $gg \to \psi(\to \mu^+\mu^-) + \gamma^*(\to \mu^+\mu^-)$ as shown in Fig. 1f, and determine its relative importance in $p\bar{p}$ collisions.

The considered subprocesses are thus:

(1), (2) : $gg/q\bar{q} \to \psi\psi$ ("direct" = g fusion/annihilation)

(3), (4) : $gg/q\bar{q} \to b\bar{b} \to \psi\psi$ (lowest order inclusive)

(5), (6) : $gg/q\bar{q} \to B_{(r)}\bar{B}_{(r)} \to \psi\psi$ (exclusive = g fusion/double recombination)

(7) : $\bar{q}g \to B_r\bar{b} \to \psi\psi$ (recombination)

(8) : $gg \to \psi\gamma^*$ (background)

where the B meson produced via recombination is given the index r.

In our subsequent calculations, the $\psi(c\bar{c})$ and $B(b\bar{q})$ mesons are treated as non-relativistic bound states. This approximation has led to sensible results in the mass spectrum[6], and is often used for cross-section estimates[5]. Each of the quarks carries the fraction $\xi_i \equiv (m_i/M)$ of the meson momentum P. The consequences of such assumptions have been analyzed earlier in Ref. 7). The set of gauge invariant graphs for each of the various subprocesses is indicated in Fig. 1. We have explicitly verified gluon gauge invariance. For the description of the non-relativistic bound state and the evaluation of parton cross-sections, we refer to Ref. 8). The longitudinal component of the gluon polarization vector was eliminated by the transverse projector as shown in Ref. 9), and the spin traces were carried out by the computer program SCHOONSHIP[10]. We have averaged over all initial and summed over all final colour states.

The parton cross-sections for "direct" $\psi\psi$ production via gluon fusion (Fig. 1a) and $q\bar{q}$ annihilation (Fig. 1b) are given by

$$\frac{d\sigma}{d\hat{t}}(gg \to \psi\psi) = \frac{3}{4\pi}\left(\frac{\pi\alpha_s}{3}\right)^4 \frac{|\psi_{(0)}|^2}{M_\psi} \frac{|\psi_{(0)}|^2}{M_\psi} \frac{\hat{s}^4 \sum_0^4 y^n C_n}{(\hat{t}-M_\psi^2)^4(\hat{u}-M_\psi^2)^4} \qquad (2.1)$$

$$\frac{d\sigma}{d\hat{t}}(q\bar{q}\to\psi\psi) = \frac{2}{3\pi}\left(\frac{16\pi\alpha_s}{3\hat{s}}\right)^4 \frac{|\psi(0)|^2}{M_\psi}\frac{|\psi(0)|^2}{M_\psi}\left[3+4y-10z^2-24z^2y-24z^4\right] \qquad (2.2)$$

where $y \equiv (\hat{t}+\hat{u})/2\hat{s}$, $z \equiv (\hat{t}-\hat{u})/2\hat{s}$ and M_ψ is the ψ rest mass. $\psi(o)$ is the bound state wave function at the origin[11]. The coefficients C_n are defined in the Appendix, Eq. (A.1). For the parton cross-sections of $gg/q\bar{q} \to b\bar{b}$ (Fig. 1c), we refer to Ref. 12).

Analogous evaluation of Figs. 1a and 1b for $B\bar{B}$ production leads to

$$\frac{d\sigma}{d\hat{t}}(gg\to B\bar{B}) = \frac{1}{2\hat{s}\pi}\left(\frac{\pi\alpha_s}{3}\right)^4 \frac{|\psi(0)|^2}{M_B}\frac{|\psi(0)|^2}{M_B}\left(\frac{1}{\xi_1\xi_2}\right)^6 \frac{\hat{s}^4\sum_{n=0}^{4}\xi_1^\ell F^{(\ell)}}{(\hat{t}-M_B^2)^4(\hat{u}-M_B^2)^4} \qquad (2.3)$$

$$\frac{d\sigma}{d\hat{t}}(q\bar{q}\to B\bar{B}) = \frac{1}{6\hat{s}\pi}\left(\frac{4\pi\alpha_s}{3\hat{s}^2}\right)^4 \frac{|\psi(0)|^2}{M_B}\frac{|\psi(0)|^2}{M_B}\left(\frac{1}{\xi_1\xi_2}\right)^6 (\hat{u}-\hat{t})^2(\hat{t}\hat{u}-M_B^4) \qquad (2.4)$$

where $\xi_i = m_i/M_B$ takes care of the mass difference between the u and the b quark. The functions $F^{(0)} \ldots F^{(4)}$ are defined in Eqs. (A.2) - (A.5).

The parton cross-section of the "double recombination" process $q\bar{q} \to B_r\bar{B}_r$ (Fig. 1d) can, with approximations, be cast in the form

$$\frac{d\sigma}{d\hat{t}}(q\bar{q}\to B_r\bar{B}_r) = \left(\frac{\pi^3\alpha_s^4}{27\hat{s}^4}\right)\frac{|\psi(0)|^4}{M_B^2}\frac{\sum_{n=0}^{6}\xi_1^n C^{(n)}}{\left[\xi_1\xi_2(v-\xi_2)^2(v-\xi_2^2)\right]^4} \qquad (2.5)$$

where the functions $C^{(n)}$ are listed in (A.6).

The parton cross-section of the (single) recombination process $\bar{q}g \to B_r\bar{b}$ (Fig. 1e) is simplified to the form

$$\frac{d\sigma}{d\hat{t}}\left(\bar{q}g \to B_r\bar{b}\right) = \frac{\pi^2\alpha_s^3}{2592\,\hat{s}^3}\,\frac{|\psi(0)|^2}{M_B^2}\,\frac{\sum_{n=0}^{10}\xi_1^n\,C^{(n)}}{\left[\,\xi_1\xi_2(v-\xi_2)(v-\xi_2^2)(u-\xi_1^2)\,\right]^2} \tag{2.6}$$

where the coefficients $C^{(n)}$ are functions of $U \equiv \hat{s}/M_B^2$, $W \equiv V-1$ with $V \equiv \hat{t}/M_B^2$, and $\xi_i = m_i/M_B$ represents the mass ratio for the heavy and light quarks. The functions $C^{(n)}$ are listed in (A.7).

The parton cross-section for the background process $gg \to \psi + \gamma^*(Q^2)$ (Fig. 1f) reads:

$$\frac{d\sigma}{d\hat{t}}\left(gg \to \psi\gamma^*\right) = \left(\frac{64\alpha}{27}\right)\left(\frac{\pi\alpha_s}{\hat{s}}\right)^2\frac{|\psi(0)|^2}{M_\psi}\,\frac{M_\psi^2\sum_{n=0}^{4}(Q^2)^n\,C^{(n)}}{\left[\hat{s}(Q^2-\hat{s}-\hat{u})(Q^2-\hat{s}-\hat{t})(2Q^2-\hat{u}-\hat{t})\right]^2} \tag{2.7}$$

where the functions $C^{(0)}\ldots C^{(4)}$ are listed in (A.9). If, in addition, $\mu^+\mu^-$ pair production is considered, the cross-section has to be multiplied by the $\psi \to \mu^+\mu^-$ branching ratio and the factor

$$BR\left(\gamma^* \to \mu^+\mu^-\right) = \left(\frac{2\alpha}{3\pi\sqrt{Q^2}}\right) \tag{2.8}$$

describing lepton-pair production by the off-shell photon.

The wave function at the origin $\psi(0)$ is for the ψ meson determined by the $\psi \to e^+e^-$ decay width Γ_e

$$|\psi(0)|^2 = \frac{M_\psi^2\,\Gamma_e}{16\pi\alpha^2 e_c^2} = 6.038 \tag{2.9}$$

e_c is the charge fraction of the charmed quark.

For the B meson its value is different. Non-relativistic model calculations reveal $|\psi(0)|^2 \sim \mu^{3/(2+\nu)}$ where μ is the reduced mass of the two-quark system[11] and $0.1 < \nu < 1$. Thus we may expect moderate variation in the mass range we consider, leaving subsequent insights pratically unchanged. In the subsequent numerical evaluation, we set $\alpha_s = 0.3$. We compare the shape and size of the parton cross-sections for $\psi\psi$ production, assuming $BR(B \to \psi + X) = 0.01$ [13] for the B branching ratio.

In Fig. 2, we expose the differential parton cross-sections $d\hat{\sigma}/d\hat{t}$ at $\hat{s} = 200\ GeV^2$. For the subprocess $q\bar{q} \to \psi\psi$ it rises with falling $\hat{t}$ to a flat plateau of $d\hat{\sigma}/d\hat{t} \sim 6.10^{-39} cm^2/GeV^2$, and decreases again towards the wide angle phase space boundary. In $gg \to \psi\psi$, we find a dip of a factor 5 in the intermediate $\hat{t}$ range; a maximum point thus appears in the upper and the lower $\hat{t}$ region. However, as the centre-of-mass energy grows, a strong rise in the forward and backward regions develops. The subprocesses $gg/q\bar{q} \to b\bar{b} \to \psi\psi$ lead to a relatively flat angular distribution around $d\hat{\sigma}/d\hat{t} \sim 10^{-37} cm^2/GeV^2$, with a valley in the intermediate $\hat{t}$ region of a factor 4.5 for gluon fusion, and a factor 1.3 for $q\bar{q}$ annihilation. The exclusive B formation $gg \to B\bar{B} \to \psi\psi$ is one and a half orders of magnitude below "direct" $\psi\psi$ production, roughly; it also vanishes at the phase space boundaries. The analogous $q\bar{q}$ annihilation process (Fig. 1b) is very small and its characteristics are therefore no longer pursued. The double recombination process $q\bar{q} \to B_r\bar{B}_r \to \psi\psi$ decreases steadily with falling $\hat{t}$. The $B(b\bar{q})$ recombination process $\bar{q}g \to B_r + \bar{b} \to \psi\psi$ leads to similar characteristics; it lies a factor 10 above the former process and its $\hat{t}$ decrease is weaker. As $|\hat{t}| \to 0$, it reaches $\sim 10^{-36} cm^2/GeV^2$ and does not diverge.

In Fig. 3, we expose the energy dependence of the integrated parton cross-sections. After the pronounced threshold onset reaching $\gtrsim 3.10^{-35} cm^2$, the "direct" processes $gg/q\bar{q} \to \psi\psi$ [(1), (2) in the earlier list] decrease rapidly. The threshold onset of all other processes is less pronounced or even extended (Process 6). At $\hat{s} = 200\ GeV^2$, typical cross-section values are:

$$\begin{aligned} \hat{\sigma}_2 \approx 2\hat{\sigma}_1 \approx 30\hat{\sigma}_5 &\cong 10^{-36} cm^2 \\ \hat{\sigma}_3 \approx \hat{\sigma}_4 \approx \hat{\sigma}_7 \approx 30\hat{\sigma}_6 &\gtrsim 10^{-35} cm^2 \end{aligned} \qquad (2.10)$$

where the index numbers refer to the earlier listed subprocesses. With increasing $\hat{s}$, the cross-sections either remain almost constant (processes 3,4,7,6) leading later to a $\hat{s}^{-1}$ decrease, or decrease more rapidly as $\hat{s}^{-3}$. The exclusive and inclusive production modes are related by a reduction factor which is determined in $e^+e^- \to B\bar{B}$. The exclusive B production is described perturbatively (analogous to Fig. 1a) [7], whereas the inclusive B production is given by $e^+e^- \to b\bar{b}$. The "branching ratio" for the exclusive $b \to B$ transition

$$BR(b \to B) = \left[\sqrt{2}\, \frac{4\pi\alpha_s}{3}\, \frac{|\psi_{10}|^2\, M_B}{m_q^2\, \hat{s}} \right] = 0.1\, \alpha_s \qquad (2.11)$$

is evaluated in the threshold region. Assuming $\alpha_s = 0.3$, we expect a factor 10^{-3} suppression if the cross-section size of subprocesses (3), (4) and (7), (8) is compared. The recombination subprocess does not follow this pattern since the exchange of a soft gluon is involved, which causes a strongly peaked angular distribution. Similar arguments apply to the double-recombination process (6). Its slow threshold onset, however, permits a comparison only at higher energies.

We add here a few remarks on the relative size of the QCD graphs in specific subprocesses, assuming that they are evaluated in the Feynman gauge.

The subprocess (6) (Fig. 1d) is fully dominated by the two shown graphs, whereas the contributions of all other graphs (squared amplitudes and interference terms) lie orders of magnitude below. This statement holds true in the region of the threshold onset, as well as for higher and even very large $\hat{s}$ values. With the above approximation, one finds in the threshold region a factor 1.5 discrepancy at most.

The subprocess (7) is fairly well represented by the first and the third graphs in Fig. 1e, since the additional $\hat{s}$ dependence in the denominator of the "u-channel" graph (second in Fig. 1e) depresses its influence by orders of magnitude.

The parton cross-sections in Eqs. (2.5) and (2.6) are obtained by assuming these simplifications. One should bear in mind that they were obtained by choosing a specific gauge.

3. - HADRONIC $\psi\psi$ PRODUCTION

The integrated cross-sections for $\psi\psi$ production in $p\bar{p}$ collisions and the kinematical distributions of the different production mechanisms are exposed in this section.

In order to determine the hadronic $\psi\psi$ production cross-sections, we fold the parton cross-sections with the scale independent parton momentum distributions. The valence and sea distributions of the proton are those of Ref. 14). The counting rule power of the gluon distribution in the nucleon is $n_G = 5$. The choice of the parton distributions and in particular their behaviour at small x values considerably influences the size of the hadronic cross-sections. The absolute value of the integrated cross-sections can therefore vary within a factor three according to the particular choice. The relative difference between the various constituent processes is, however, much less affected. The main features of the differential distributions remain almost unchanged by this ambiguity. We have explicitly verified that in the mass range we consider, scaling violation does not affect the results in a crucial way.

In Fig. 4, we show the energy dependence of the integrated cross-sections following from the constituent processes (1)-(8). Several characteristics are observed:

(a) At $\sqrt{s} = 540$ GeV, the dominating constituent mechanisms for $\psi\psi$ production are: $gg \to \psi\psi$, $gg \to b\bar{b} \to \psi\psi$ and $\bar{q}g \to B_r\bar{b} \to \psi\psi$. They are roughly of equal size: $\sigma \sim 4.10^{-34}\text{cm}^2$, leading to an estimated overall cross-section of $\sigma_{\psi\psi} \gtrsim 10^{-33}\text{cm}^2$. Since all processes are initiated by anti-quarks or gluons, one may not expect substantially different rates by choosing different hadrons in the initial state. Since the rise (or levelling off) of the curves is significantly correlated with the low x behaviour of the momentum distributions, one may not expect a significant rise of the $\psi\psi$ production rate by going to even higher energies.

(b) Our model calculations indicate (at $\sqrt{s} = 540$ GeV) that a substantial fraction of the $\psi\psi$ events originate from $b\bar{b}$ production with consequent $b \to \psi + X$ decay. The significance of such a mode of production has been evoked earlier (though at lower energies)[4], and now finds its likely realization at collider energies. We furthermore notice that the recombination process (7) is of considerable importance, although the uncertainties due to the size of the bound state wave function at the origin, together with the simplicity of the model, should be kept in mind here. Exclusive $B\bar{B}$ production with subsequent $B \to \psi + X$ decay may be ignored as compared to the inclusive production modes.

(c) At lower energies ($\sqrt{s} \lesssim 40$ GeV), "direct" $\psi\psi$ production via the constituent processes (1) and (2) dominates, whereas the other investigated processes may be ignored. All mechanisms for inclusive b production [(3), (4) and (7)] lead to roughly the same cross-sections in the lower energy range.

(d) In order to get an estimate of the size of the background, we have determined the size of the integrated cross-section following from the constituent process $gg \to \psi(\hookrightarrow \mu^+\mu^-) + \gamma^*(\hookrightarrow \mu^+\mu^-) + X$, which acts as one of the main background sources to $\psi(\hookrightarrow \mu^+\mu^-) + \psi(\hookrightarrow \mu^+\mu^-)$ production. In order to expose the relative size of the cross-sections, we show in Fig. 4, by curve 8, the quantity

$$\bar{\sigma}_{\psi\gamma^*} \equiv \sigma\left(p\bar{p} \to \psi_{\hookrightarrow \mu^+\mu^-} + \gamma^*_{\hookrightarrow \mu^+\mu^-}\right) \left[\frac{1}{BR(\psi \to \mu^+\mu^-)}\right]^2 \qquad (3.1)$$

We thus conclude that this background process is quite small, though it is still more important than $\psi\psi$ production via the exclusive $B\bar{B}$ production modes.

In Fig. 5, we show the (centre-of-mass) rapidity distribution of one single ψ. The relative size of the integrated cross-sections is again found in this distribution. During a relatively wide y range ($-2 \leq y_1 \leq +2$), it is flat without much variation and shows the typical fall-off for $y_1 > 2.5$. Note in particular that in this region the two subprocesses $gg/q\bar{q} \to \psi\psi$ become of equal importance, whereas the influence of the subprocesses (3) and (4) diminishes.

In Fig. 6, we illustrate the cross-section behaviour for increasing p_t. After the initial rise, the subprocesses (1) and (2) reach their maxima around $p_t \sim 1.2$ GeV, and subsequently fall off exponentially. The maximum point for the subprocesses (3) and (4) is at $p_t \sim 2.5$ GeV and the fall-off with increasing p_t is slow. By imposing a p_t cut-off at $p_t \simeq 3$ GeV, one can therefore fully eliminate the "direct" constituent processes (1) and (2), and focus on the $\psi\psi$ production modes via the B meson.

The double rapidity distributions in Figs. 7a-7c expose the correlations between the two ψ's. Consider Fig. 7a, where $y_1 = 0$ and y_2 = variable is imposed. Beyond $y_2 > 1.5$, the cross-section is dominated by the constituent processes (3) and (7), thus the "direct" production modes are eliminated by this constraint. At $y_2 \sim 0$, the "direct" and b quark production modes are expected to be of equal importance. Choosing instead $y_1 = y_2$, as shown in Fig. 7b,

"direct" $\psi\psi$ production is favoured at large rapidities ($y_2 > 3$), since $\psi\psi$ production bends off earlier and faster towards small cross-section values via the b quark. For all constituent processes, the rapidity distribution here is almost constant over a long y range. The constraint $y_1 = -y_2$, with the cross-section predictions given in Fig. 7c, reveals a predominance of the constituent processes (3) and (7) already at quite low rapidity values ($y_2 \geq 0.75$). Comparing Figs. 7b and 7c, one notices that the two ψ's emerge more favourably in the same direction than with their momenta pointing in opposite directions. This is easily understood by the fact that the quark masses may be ignored as compared to the available CM-energy, and consequently any Lorentz transformation from the constituent CM-system to the $p\bar{p}$ CM-system bends both ψ's either forwards or backwards.

In Fig. 8, we show the differential cross-section as a function of the rapidity of the $\psi\psi$ system. The characteristics of the curves are very similar to those of Fig. 7b, where $y_1 = y_2$ is imposed. At large y_2, in particular, the "direct" $\psi\psi$ production mechanism dominates.

The distribution in the invariant mass of the $\psi\psi$ system, illustrated by Fig. 9, is an excellent means of focusing on the "direct" or the "B meson" production modes. If $\psi\psi \lesssim 9$ GeV is imposed, the constituent processes $gg/q\bar{q} \rightarrow$ $\rightarrow \psi\psi$ dominate $\psi\psi$ production, whereas at $M_{\psi\psi} \gtrsim 11$ GeV the subprocess $gg \rightarrow$ $\rightarrow b\bar{b} \rightarrow \psi\psi$ is most important, with the recombination process $\bar{q}g \rightarrow B_r\bar{b} \rightarrow \psi\psi$ being of roughly equal size. The differential distribution $d\sigma/dM$ exposes essentially the $\hat{s}$ fall-off of the integrated constituent cross-sections as shown in Fig. 3. By measuring the $M_{\psi\psi}$ distribution, one determines their fall-off: $\hat{\sigma} \sim \hat{s}^{-n} \cdot$ const, since the variation due to the parton momentum distributions is in the $\hat{s}$ threshold region of minor importance. One expects $n = 3$ for the "direct" processes (1) and (2) and $n \simeq 1$ for the $\psi\psi$ production via the B meson.

We have also defined the x_F distributions (instead of y) of single and double ψ production, and conclude from this analysis that they do not allow for a good distinction between the various production mechanisms.

4. - QUARK MASS DEPENDENCE

In the preceding sections, we have determined the cross-sections for heavy meson production in $p\bar{p}$ collisions based on low-order QCD models where all quarks are on-shell. One of the characteristics of these models is hidden in their dependence on the heavy quark masses which we aim to expose in this section.

Choosing $\sqrt{s}$ = 540 GeV, we have determined the variation of the different cross-sections contributing to $p\bar{p} \to \psi\psi + X$ as a function of the heavy quark mass m_c in the case of "direct" $\psi\psi$ production [processes (1) and (2)], and as a function of the heavy quark mass m_b in all other constituent processes. All other parameters are kept fixed for the moment. In particular, we exclude any variation of the bound state wave function at the origin $|\psi(o)|^2$, and do not allow for any M dependence in the running coupling constant. We have furthermore ignored the scale dependence of the momentum distributions which at lower masses is a valuable approximation.

The results of this analysis are presented in Figs. 10-12 (dashed curves). Instead of the heavy quark mass, we have varied the mass of the produced meson M. For "direct" $\psi\psi$ production (Fig. 10a), a strong decrease is observed, since two pairs of c quarks must be generated. The propagator denominator of the hard gluon line, responsible for the creation of the second $c\bar{c}$ pair, is at the origin of their rapid decrease. As a result, the cross-section for $\psi\psi$ production, or quark-antiquark bound states of even higher masses, will be almost unmeasurably small. The cross-section fall-off for $b\bar{b}$ production (Fig. 11) is weakest, since there is no hard gluon line for the production of another heavy quark pair. One notices a slight difference between the gg and $q\bar{q}$ initiated subprocesses, which we attribute to the low x fall-off of the momentum distributions. The M fall-off of the recombination process (7) (Fig. 12) lies in between the two earlier types of processes.

A simple fit near the meson masses gives the following power decrease:

$$\begin{aligned} \sigma(gg/q\bar{q} \to \psi\psi) &\propto M^{-8.1}, M^{-7.8} \\ \sigma(gg/q\bar{q} \to b\bar{b} \to \psi\psi) &\propto M^{-2.6}, M^{-2.0} \\ \sigma(\bar{q}g \to B_r\bar{b} \to \psi\psi) &\propto M^{-3.72} \end{aligned} \tag{4.1}$$

The approximations mentioned earlier are, however, of importance for a comparison with the experimental data on c and b quark meson production. In Fig. 10b, we expose the changes as we gradually vary the parameters. Whilst determining the (dashed) line 1, we have assumed the gluon distribution

$$xG(x) = 0.4\,(n_g+1)\,(1-x)^{n_g} \tag{4.2}$$

with $n_g = 5$. Variation of n_g within the range $3 \leq n_g \leq 11$ reveals a modest effect (curves 2). Seeking an estimate of the (leading log) QCD corrections to the lowest order processes (1)-(7), we have used the AF parametrization of Ref. 15). Curve 3 results from the scale in the structure functions, with $\alpha_s = 0.3$, however, kept fixed. Note that there is almost no dependence on the scale parameter $0.2 \leq \Lambda \leq 0.5$ GeV. The same analysis, with a running coupling constant in the lowest order parton cross-sections: $\alpha_s(M^2) = (12 \cdot \pi/25) \cdot (1/\log(M^2/\Lambda^2))$ leads to curve 4 (curve 5), where $\Lambda = 0.2$ ($\Lambda = 0.5$) is used. The QCD corrections thus lead to a stronger fall-off with increasing M.

In a successive step, the bound state wave function at the origin is varied, assuming[11]

$$|\psi_a|^2 = |\psi_c|^2 \left[\frac{M_a}{M_\psi} \right]^{3/2+\nu} \tag{4.3}$$

with $|\psi_c|^2$ given in Eq. (2.9) and ν variation as $0.1 \leq \nu \leq 1$. The resulting M decreases are indicated by the solid lines in Figs. 10-12.

Considering the amount of uncertainties in the above investigation, we conclude that exact predictions for the cross-section size of heavy quark production is not possible. The kinematical distributions, however, reveal characteristic information which is a direct consequence of the input assumptions.

5. - SUMMARY

The preceding study is intended as an exploratory evaluation of the cross-section size and the characteristic kinematical distributions of $\psi\psi$ production in $p\bar{p}$ collisions at $\sqrt{s} = 540$ GeV. Our results are summarized as follows:

1) The integrated cross-section for $p\bar{p} \to \psi\psi + X$ is above 10^{-33}cm^2.

2) A large fraction of the events is due to "direct" production and via B meson intermediate states (although other mechanisms such as χ production cannot be excluded).

3) The two mechanisms can be separated by imposing cuts in the invariant mass distribution of the $\psi\psi$ system $M_{\psi\psi}$, or by choosing appropriate kinematical regions in the rapidity variables or in the transverse momentum.

4) The $M_{\psi\psi}$ distribution gives direct insight into the $\hat{s}$ fall-off of the integrated parton cross-sections.

5) The B meson production via the recombination $\bar{q}g \to B_r + \bar{b}$ is likely to be an important constituent process. Its size, however, depends on the bound state wave function at the origin $|\psi(o)|^2$ which is not sufficiently known for precise predictions.

6) We have determined the dependence of the $\psi\psi$ cross-section on the heavy quark mass which allows predictions on the cross-section size for mesons involving even heavier quarks.

ACKNOWLEDGEMENTS

We thank J. Ellis, M. Jacob and E. Reya for fruitful discussions. One of us (B.H.) thanks Professor C. Joseph for his kind help.

APPENDIX

Expansion coefficients for the parton cross-section in Eq. (2.1).

```
C (0) = (3981312*Z12+258048*Z10-1186048*Z8+35584*Z6+98144*Z4-13568*Z2+335)*(2/3)
C (1) = (1935360*Z10-596224*Z8-403840*Z6+168064*Z4-14288*Z2+137)*(8/3)
C (2) = (1134336*Z8-1010944*Z6+239008*Z4-11472*Z2-1)*(8/3)
C (3) = (-10176*Z6+688*Z4+828*Z2+5)*(64/3)
C (4) = (16*Z4+8*Z2+1)*256
```
(A.1)

where the shorthand notation $Z5 \equiv Z^5$, etc., is used.

Expansion coefficients for the parton cross-section in Eq. (2.3). The first three of the functions $F^{(0)} \ldots F^{(4)}$ have the structure

$$F^{(\ell)}(y,z) = \sum_{n=0}^{4} y^n \, C_n^{(\ell)}(z) \qquad (\ell = 0,1,2) \qquad (A.2)$$

with the coefficients C_n given by

```
C0 (0) = (20736*Z12+18432*Z10+6688*Z8-2592*Z6-1003*Z4+88*Z2+32)/32
C0 (1) = (9792*Z10+7952*Z8-20*Z6-1325*Z4-22*Z2+48)/4
C0 (2) = (4112*Z8+1816*Z6-847*Z4-174*Z2+52)
C0 (3) = (208*Z6-8*Z4-35*Z2+6)*16
C0 (4) = (16*Z4-8*Z2+1)*64
```
(A.3)

```
C1 (0) = (-94464*Z10-63872*Z8-2240*Z6+11192*Z4+325*Z2-404)/32
C1 (1) = (-76032*Z10-212864*Z8-66048*Z6+38328*Z4+6745*Z2-2144)/16
C1 (2) = (-32640*Z8-37936*Z6+6912*Z4+5253*Z2-1025)/2
C1 (3) = (-10128*Z6-2192*Z4+2857*Z2-419)*2
C1 (4) = (-528*Z4+256*Z2-31)*16
```
(A.4)

```
C2 (0) = (377856*Z10+768768*Z8+130048*Z6-94720*Z4-25732*Z2+6981)/128
C2 (1) = (152064*Z10+855040*Z8+543360*Z6-132080*Z4-79546*Z2+16227)/32
C2 (2) = (883968*Z8+1722880*Z6+12256*Z4-348512*Z2+56181)/32
C2 (3) = (188736*Z6+96784*Z4-78164*Z2+10575)/4
C2 (4) = (25872*Z4-12280*Z2+1457)
```
(A.5)

where the shorthand notation $Z10 \equiv Z^{10}$, etc., is used. The remaining two follow from the $\xi_1 \leftrightarrow \xi_2 \equiv 1-\xi_1$ symmetry of the cross-section: $F^{(3)} = -(F^{(1)}+F^{(2)})$, $F^{(4)} = (F^{(1)}+F^{(2)})$.

Expansion coefficients for the parton cross-section in Eq. (2.5).

```
C (0) = (32*U3*(-V3+107*V2-1411*V+729)+32*U2*(17*V4-690*V3-352*V2+2706*V-1681)
        +288*U*(-7*V5-54*V4+286*V3-464*V2+321*V-82)+2592*(-V6+6*V5-15*V4+20*V3-15*V2+6*V-1))/81
C (1) = (64*U3*(2*V3-367*V2+2696*V-2187)+128*U2*(-8*V4+465*V3+676*V2-3183*V+2050)
        +576*U*(-2*V5+68*V4-497*V3+1103*V2-977*V+305)+25920*(-V5+5*V4-10*V3+10*V2-5*V+1))/81
C (2) = (32*U3*(4*V3+529*V2-2594*V+3645)+64*U2*(-22*V4-570*V3-877*V2+4044*V-2719)
        +96*U*(-16*V5-13*V4+1131*V3-3887*V2+4513*V-1728)+864*(2*V5-47*V4+168*V3-242*V2+158*V-39))/27
C (3) = (128*U3*(-8*V3-278*V2+1357*V-3645)+128*U2*(-8*V4+672*V3+937*V2-6252*V+4219)
        +1152*U*(-10*V4-112*V3+813*V2-1304*V+613)+10368*(4*V4-31*V3+69*V2-61*V+19))/81
C (4) = (32*U3*(-64*V3-136*V2-2347*V+10935)+32*U2*(-64*V4-888*V3-1171*V2+15756*V-9529)
        +288*U*(16*V4+31*V3-1428*V2+3239*V-1858)+2592*(-V4+46*V3-168*V2+202*V-79))/9          (A.6)
C (5) = (64*U3*(16*V2+58*V-243)+128*U2*(8*V3+16*V2-170*V+77)
        +192*U*(2*V3+52*V2-173*V+119)+1728*(-V3+9*V2-15*V+7))/9
C (6) = 32*U3*(-4*V+9)+64*U2*(-2*V2+7*V-2)+96*U*(-V2+5*V-4)+288*(-V2+2*V-1)
```

where U and V are defined in Eq. (A.8).

Expansion coefficients for the parton cross-section in Eq. (2.6).

```
C ( 0) = 16*U4*W*(289*W-336)+16*U3*W*(289*W2+34*W-416)+16*U2*W3*(81*W-416)+1296*U*W5
C ( 1) = 64*U4*(-68*W2+389*W-168)+16*U3*(-578*W3+1057*W2+1656*W-576)
        +16*U2*W2*(-468*W2+981*W-1102)+288*U*W4*(-9*W+53)
C ( 2) = 32*U4*(32*W2-697*W+1146)+64*U3*(52*W3-749*W2+71*W+738)
        +4*U2*W*(1224*W3-10261*W2+13704*W+1312)+8*U*W3*(324*W2-2583*W+7991)-648*W5
C ( 3) = 1600*U4*(4*W-21)+32*U3*(1014*W2-2867*W-1434)+64*U2*(739*W3-1656*W2+90*W+306)
        +32*U*W2*(729*W2-2934*W+3235)+144*W4*(-18*W-43)
C ( 4) = 16*U4*(-64*W+561)+48*U3*(-176*W2+1623*W-838)+8*U2*(-2600*W3+15057*W2-11234*W-9792)   (A.7)
        +4*U*W*(-4320*W3+17081*W2-53844*W+12664)+8*W3*(-324*W2-2277*W-2380)
C ( 5) = 16*U3*(-1418*W+3885)+32*U2*(-2558*W2+4426*W+2499)+16*U*W*(-5024*W2+9465*W-10278)
        +32*W2*(-171*W2-1161*W-578)
C ( 6) = 96*U3*(32*W-187)+4*U2*(5768*W2-22197*W-408)+8*U*W*(4564*W2-13676*W+22273)
        +8*W2*(1548*W2+2573*W-2516)
C ( 7) = 16*U2*(1636*W-1785)+16*U*W*(5434*W-5727)+16*W2*(2322*W+2501)
C ( 8) = 48*U2*(-64*W+187)+4*U*W*(-6224*W+8297)+8*W2*(-2380*W+2089)
C ( 9) = -9888*U*W-33184*W2
C (10) =  1024*U*W+9248*W2
```

where

$$U \equiv \frac{\hat{s}}{M_B^2} \quad , \quad V \equiv \frac{\hat{t}}{M_B^2} \quad , \quad W \equiv V - 1 \qquad \text{(A.8)}$$

and the shorthand notation U7 ≡ U^7, etc., is used.

Expansion coefficients for the parton cross-section in Eq. (2.7)

```
C (0) = (S*(T+U))**2 + (U*(S+T))**2 + (T*(S+U))**2
C (1) = (T*U/M)**2 - 2*S*(U**2+T**2) - 5*S**2*(U+T) - 4*U*T*(U+T) - 14*S*T*U + S**3
C (2) = -2*(U*T/M**2)*(U+T) + 2*(U**2+T**2) + 8*T*U + 11*S**2 + 12*S(U+T)
C (3) =  2*T*U/M**2 - 3*(U+T) + 11*S
C (4) =  1
```

(A.9)

REFERENCES

1) NA3 Collaboration, Phys. Lett. 114B (1982) 457.

2) a) V. Barger, F. Halzen and W.Y. Keung, Madison preprint MAD/PH/64 (1982);
b) R.E. Ecclestone and D.M. Scott, Phys. Lett. 120B (1983) 237; DAMTP preprint 82/31 (1982).

3) B. Humpert and P. Méry, Phys. Lett. B124 (1983) 265.

4) H. Fritzsch, Phys. Lett. 86B (1979) 164, 343.

5) S.J. Brodsky and J.F. Gunion, Phys. Rev. Lett. 37 (1976) 402;
J.F. Gunion, Proceedings of the XIth Multiparticle Symposium, Brugge (1980), eds. E. DeWolf and F. Verbeure, Universitaire Instelling Antwerpen (1980) p. 767.

6) S. Ono, Aachen preprint (1982).

7) B. Humpert and R. Clark, Phys. Rev. D16 (1977) 1327;
H.F. Jones, CERN preprint TH. 3257 (1982).

8) C.H. Chang, Nuclear Phys. B172 (1980) 425;
J.H. Kühn et al., Nuclear Phys. B157 (1979) 125.

9) V.M. Budnev et al., Phys. Reports 15C (1975) 183;
R. Cutler and D. Sivers, Phys. Rev. D17 (1978) 196.

10) SCHOONSHIP - created by M. Veltman;
M. Strubbe, Computer Physics Communications 8 (1974) 1.

11) C. Quigg and J.L. Rosner, Phys. Reports 56 (1979) 167.

12) C. Michel and R. Winder, Nuclear Phys. B173 (1980) 59.

13) The CLEO Collaboration, D. Andrews et al., Preprint CNLS 82/547 (August 1982).

14) K.P. Das and R.C. Hwa, Phys. Lett. 68B (1977) 459.

15) J.F. Owens and E. Reya, Phys. Rev. D17 (1978) 3003.

FIGURE CAPTIONS

Fig. 1 : a) Order α_s^4 QCD graphs for $gg \to \psi\psi$. There are 36 graphs altogether, some of them vanishing due to colour conservation, and others are related by crossing symmetry.

b) Order α_s^4 QCD graphs for $q\bar{q} \to \psi\psi$ (two graphs).

c) Lowest order graphs for $gg/q\bar{q} \to b\bar{b} \to \psi\psi$.

d) Order α_s^4 QCD graphs for $q\bar{q} \to B_r\bar{B}_r \to \psi\psi$. B production by double recombination (seven graphs).

e) Order α_s^3 QCD graphs for $\bar{q}g \to B_r + \bar{b}$. B production by recombination (three graphs).

Fig. 2 : Differential cross-sections $d\hat{\sigma}/d\hat{t}$ of the constituent processes (1)-(7).

Fig. 3 : Integrated cross-sections $\hat{\sigma}(\hat{s})$ of the constituent processes (1)-(7).

Fig. 4 : Integrated cross-sections for $\psi\psi$ production in $p\bar{p}$ collisions of the constituent processes (1)-(8).

Fig. 5 : Single ψ rapidity distribution for the constituent processes (1)-(7) of $p\bar{p} \to \psi\psi + X$.

Fig. 6 : p_t distribution for the constituent processes (1)-(7) of $p\bar{p} \to \psi\psi + X$.

Fig. 7 : Double rapidity distribution of the constituent processes (1)-(7) contributing to $p\bar{p} \to \psi\psi + X$; the constraints a) $y_1 = 0$, y_2 variable; b) $y_1 = y_2$ variable; and c) $y_1 = -y_2$ variable reveal the correlations between the two ψ's.

Fig. 8 : Rapidity distribution of the $\psi\psi$ system.

Fig. 9 : Invariant mass distribution of the $\psi\psi$ system.

Fig. 10 : ψ mass extrapolation of the "direct" $\psi\psi$ production cross-section:
a) dependence on the bound state wave function,
b) influence of the gluon distribution and details of the QCD corrections.

Fig. 11 : B meson mass extrapolation of the $\psi\psi$ production cross-section via the constituent processes $gg/q\bar{q} \to b\bar{b} \to \psi\psi$.

Fig. 12 : B meson mass extrapolation of the $\psi\psi$ cross-section via the recombination process $\bar{q}g \to B_r + \bar{b} \to \psi\psi$.

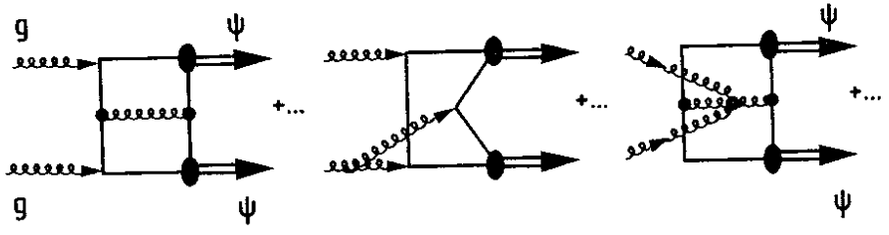

FIG. 1a

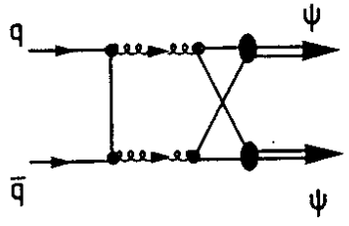

FIG. 1b

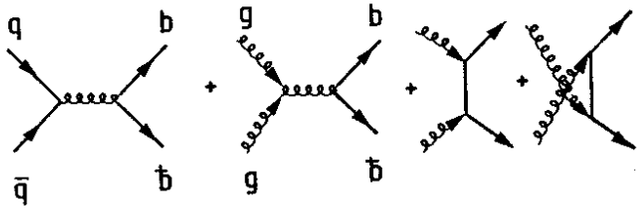

FIG. 1c

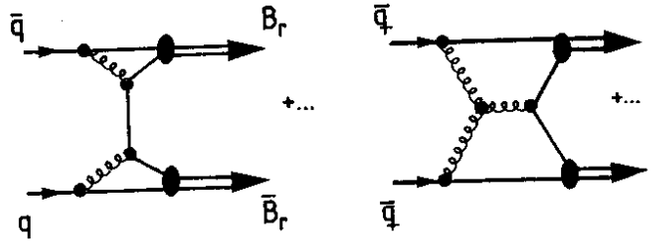

FIG. 1d

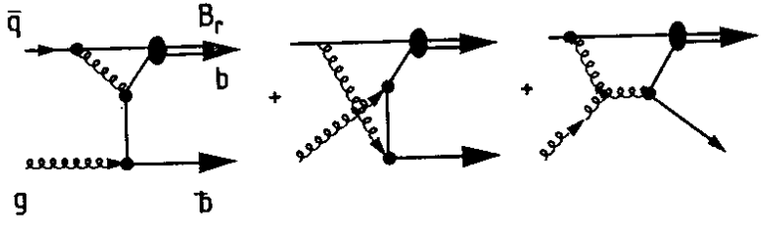

FIG. 1 e

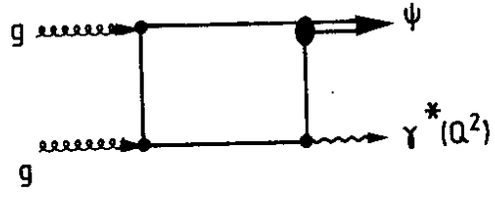

FIG. 1f

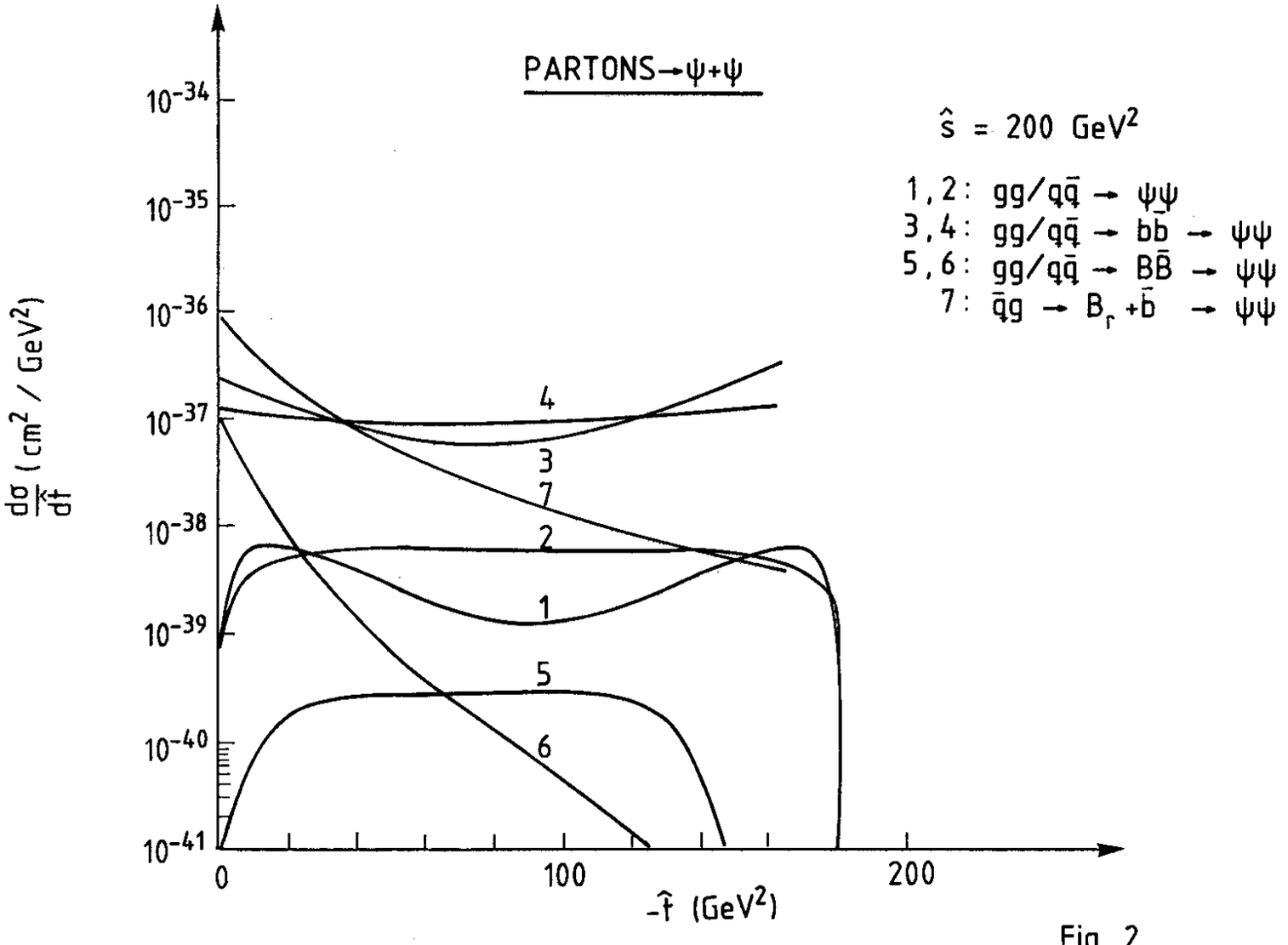
PARTONS→ψ+ψ
ŝ = 200 GeV²
1,2: gg/qq̄ → ψψ
3,4: gg/qq̄ → bb̄ → ψψ
5,6: gg/qq̄ → BB̄ → ψψ
7: q̄g → B_r + b̄ → ψψ
dσ/dt̂ (cm² / GeV²)
10⁻³⁴
10⁻³⁵
10⁻³⁶
10⁻³⁷
10⁻³⁸
10⁻³⁹
10⁻⁴⁰
10⁻⁴¹
0
100
200
-t̂ (GeV²)
1
2
3
4
5
6
7

Fig. 2

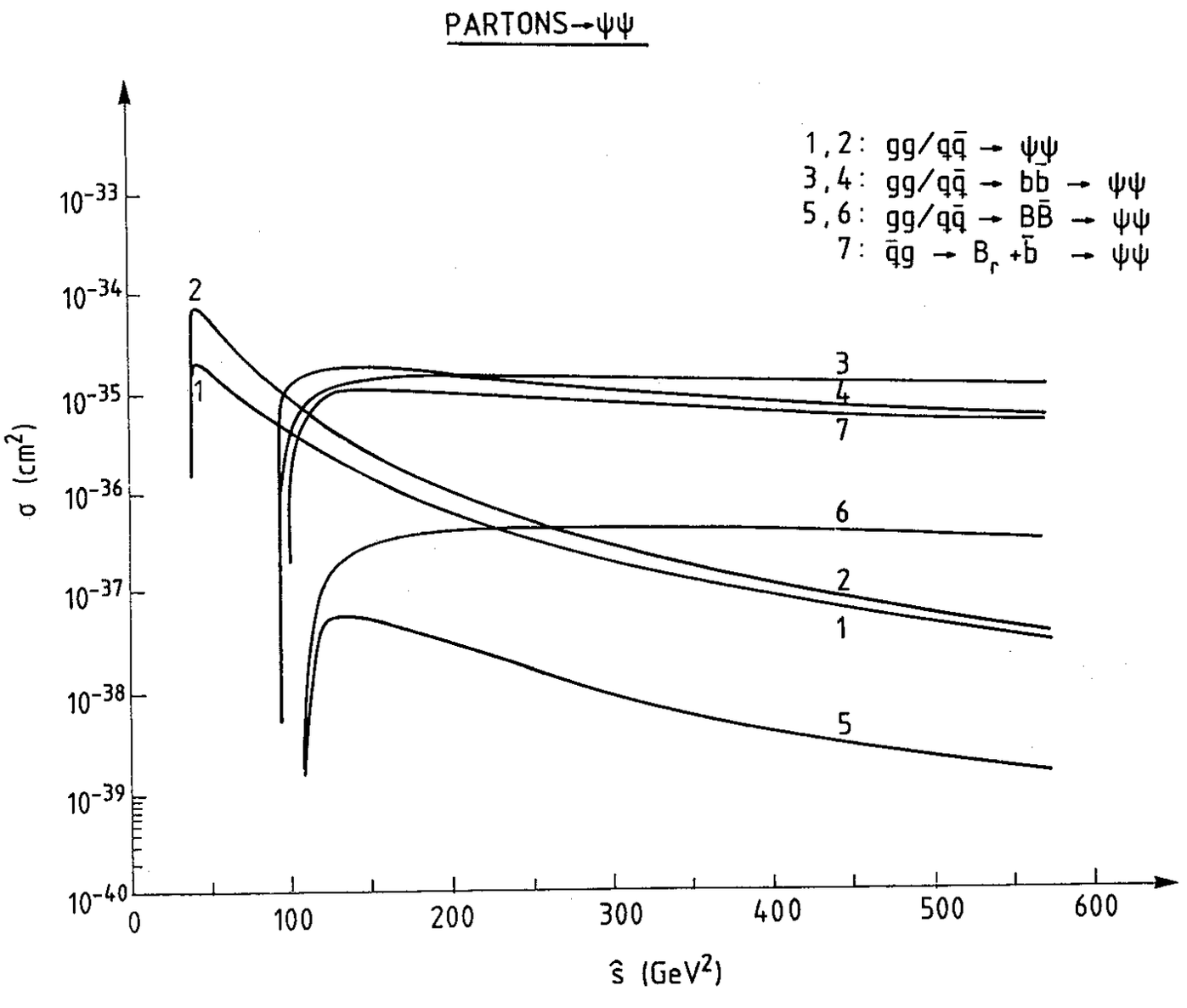
PARTONS→ψψ
1,2: gg/qq̄ → ψψ
3,4: gg/qq̄ → bb̄ → ψψ
5,6: gg/qq̄ → BB̄ → ψψ
7: q̄g → B_r + b̄ → ψψ
σ (cm²)
10⁻³³
10⁻³⁴
10⁻³⁵
10⁻³⁶
10⁻³⁷
10⁻³⁸
10⁻³⁹
10⁻⁴⁰
0
100
200
300
400
500
600
ŝ (GeV²)
1
2
3
4
5
6
7

Fig. 3

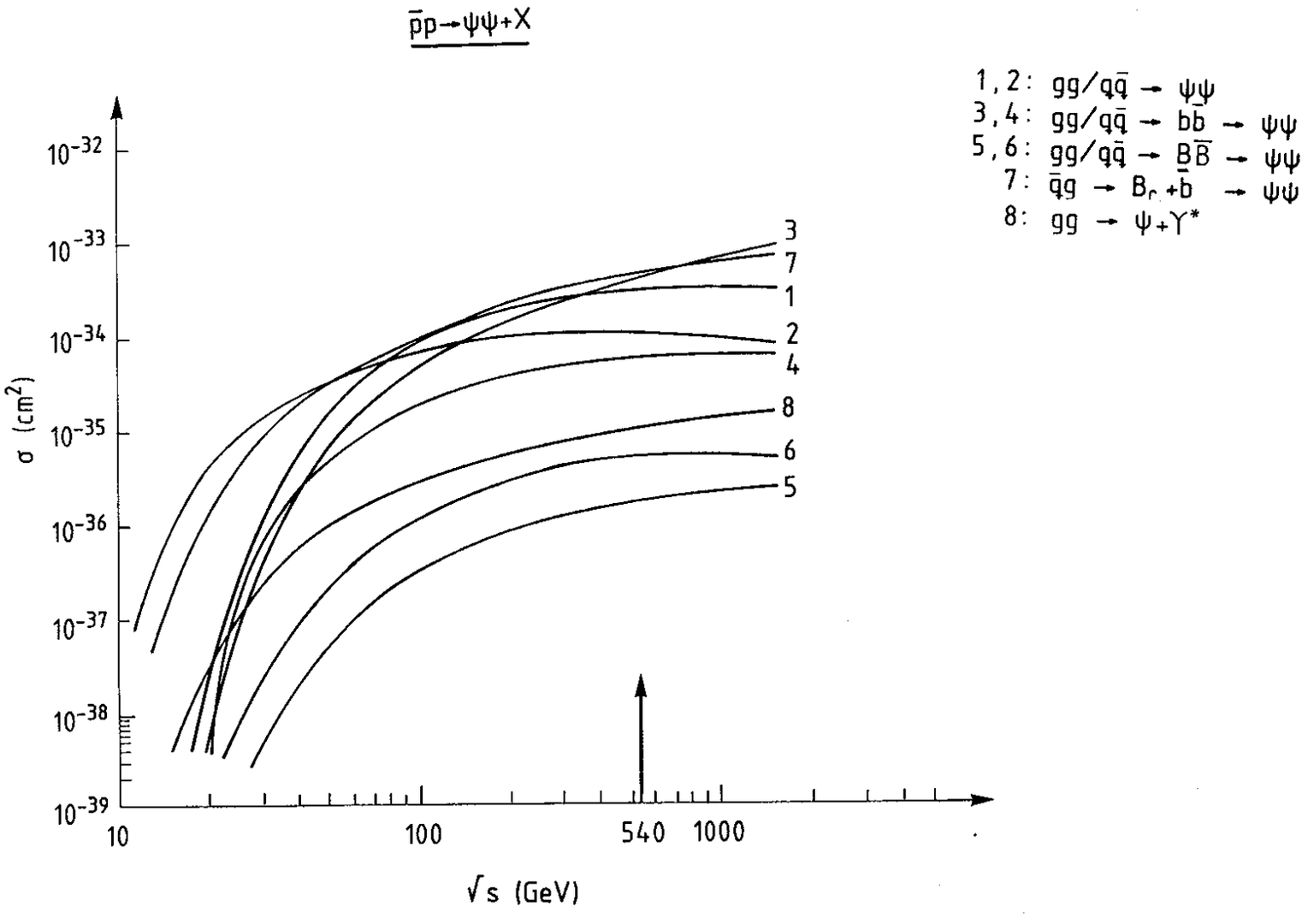
$\bar{p}p \to \psi\psi + X$
1, 2: $gg/q\bar{q} \to \psi\psi$
3, 4: $gg/q\bar{q} \to b\bar{b} \to \psi\psi$
5, 6: $gg/q\bar{q} \to B\bar{B} \to \psi\psi$
7: $\bar{q}g \to B_c + \bar{b} \to \psi\psi$
8: $gg \to \psi + \Upsilon^*$
σ (cm^2)
10^{-32}
10^{-33}
10^{-34}
10^{-35}
10^{-36}
10^{-37}
10^{-38}
10^{-39}
10
100
540
1000
$\sqrt{s}$ (GeV)
3
7
1
2
4
8
6
5

Fig. 4

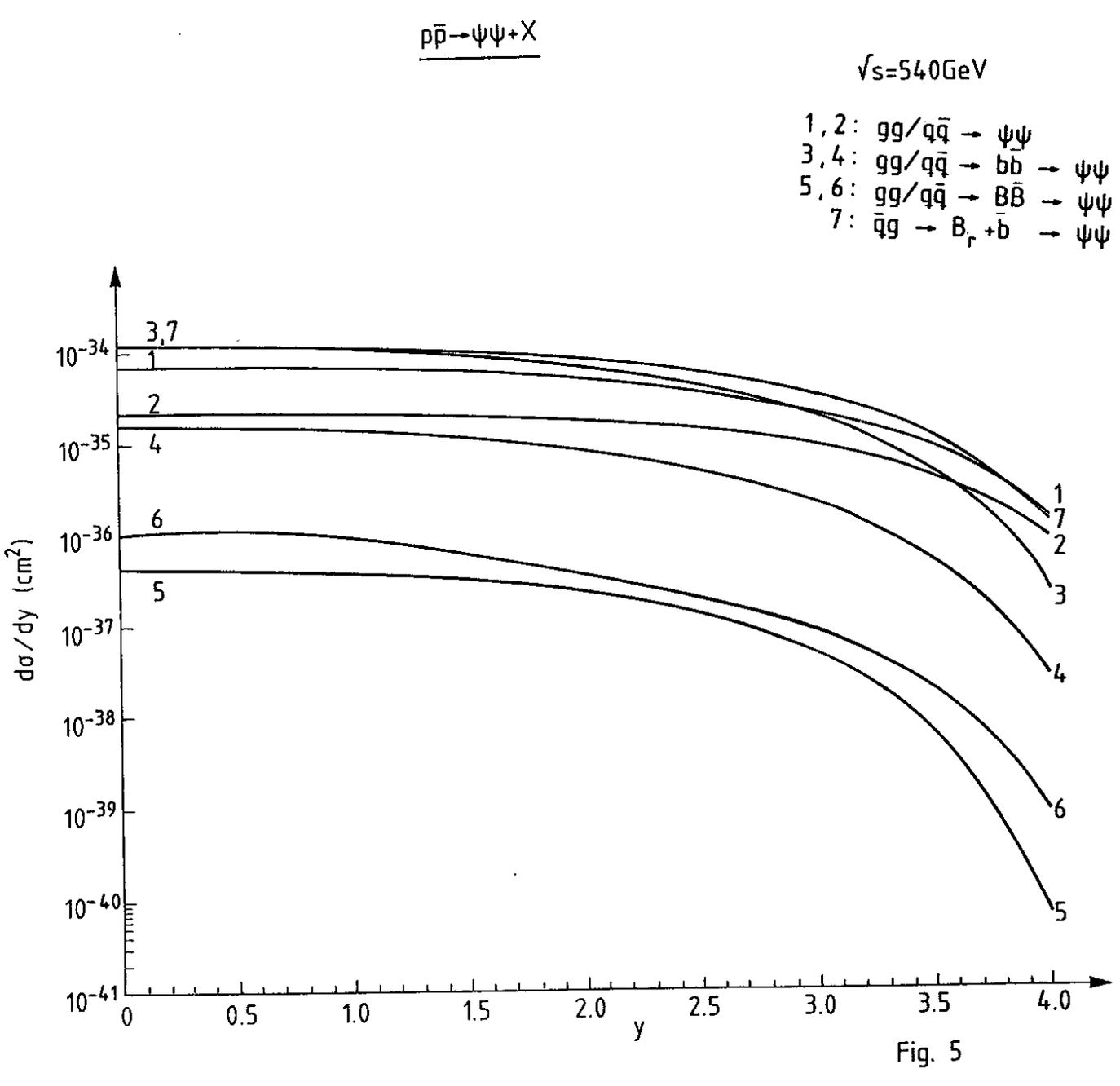
$p\bar{p} \to \psi\psi + X$
$\sqrt{s} = 540\,GeV$
1, 2: $gg/q\bar{q} \to \psi\psi$
3, 4: $gg/q\bar{q} \to b\bar{b} \to \psi\psi$
5, 6: $gg/q\bar{q} \to B\bar{B} \to \psi\psi$
7: $\bar{q}g \to B_r + \bar{b} \to \psi\psi$
$d\sigma/dy$ (cm^2)
10^{-34}
10^{-35}
10^{-36}
10^{-37}
10^{-38}
10^{-39}
10^{-40}
10^{-41}
0
0.5
1.0
1.5
2.0
2.5
3.0
3.5
4.0
y
3,7
1
2
4
6
5
1
7
2
3
4
6
5

Fig. 5

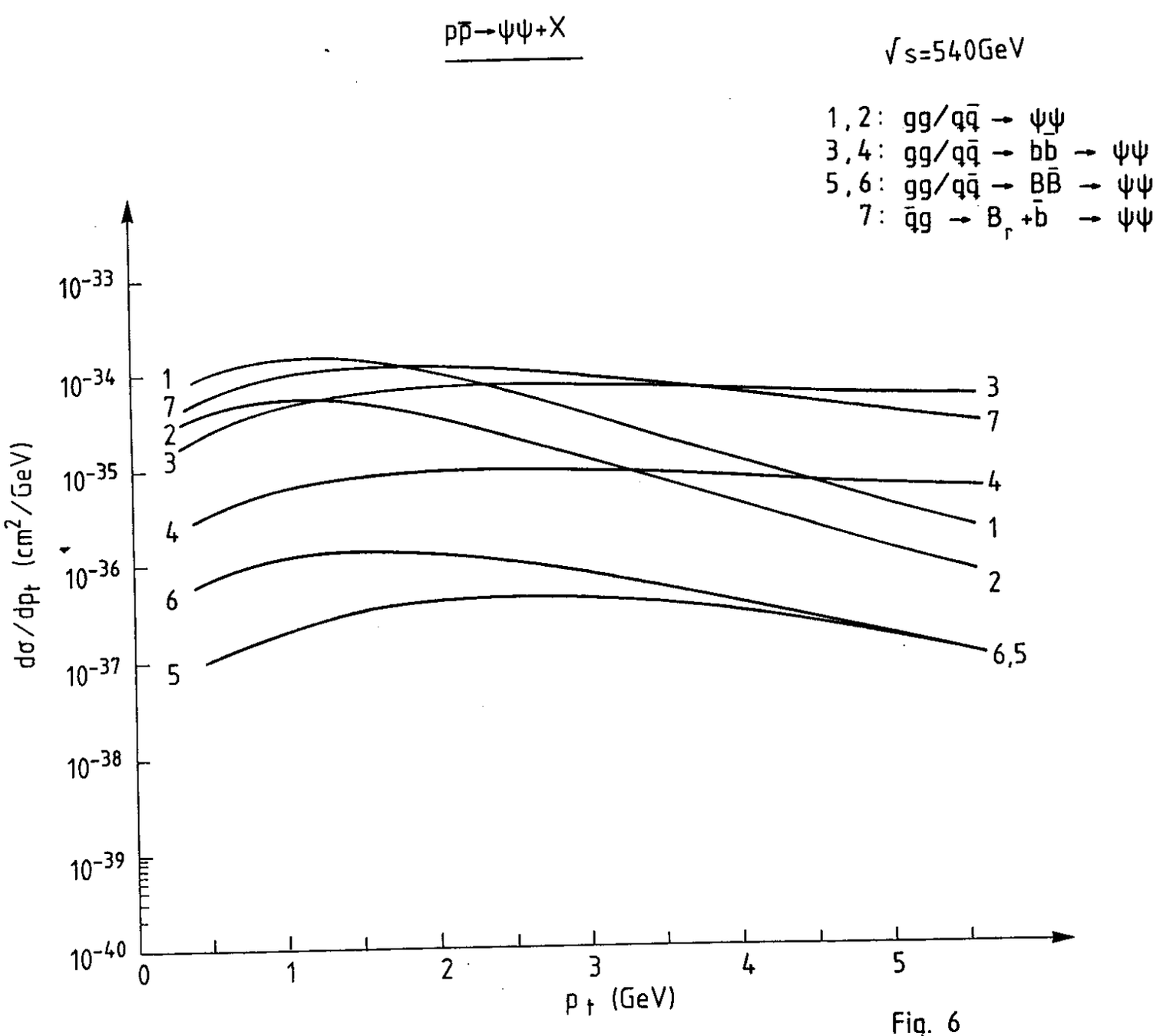
$p\bar{p} \to \psi\psi + X$
$\sqrt{s} = 540\,GeV$
1, 2: $gg/q\bar{q} \to \psi\psi$
3, 4: $gg/q\bar{q} \to b\bar{b} \to \psi\psi$
5, 6: $gg/q\bar{q} \to B\bar{B} \to \psi\psi$
7: $\bar{q}g \to B_r + \bar{b} \to \psi\psi$
$d\sigma/dp_t$ (cm^2/GeV)
10^{-33}
10^{-34}
10^{-35}
10^{-36}
10^{-37}
10^{-38}
10^{-39}
10^{-40}
0
1
2
3
4
5
p_t (GeV)
1
7
2
3
4
6
5
3
7
4
1
2
6,5

Fig. 6

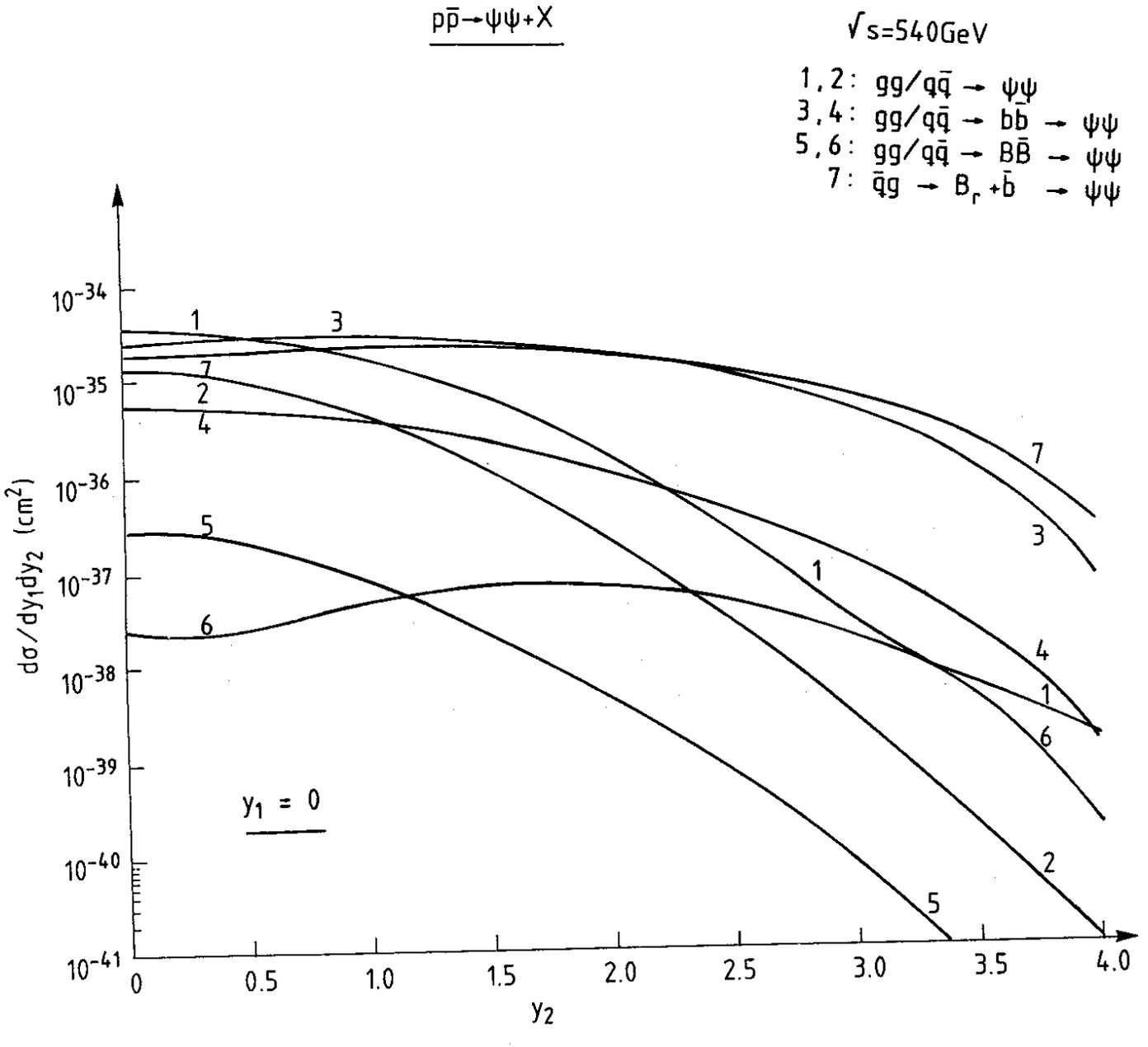
$p\bar{p} \to \psi\psi + X$
$\sqrt{s} = 540\,GeV$
1, 2: $gg/q\bar{q} \to \psi\psi$
3, 4: $gg/q\bar{q} \to b\bar{b} \to \psi\psi$
5, 6: $gg/q\bar{q} \to B\bar{B} \to \psi\psi$
7: $\bar{q}g \to B_r + \bar{b} \to \psi\psi$
$d\sigma/dy_1dy_2$ (cm^2)
10^{-34}
10^{-35}
10^{-36}
10^{-37}
10^{-38}
10^{-39}
10^{-40}
10^{-41}
$y_1 = 0$
0
0.5
1.0
1.5
2.0
2.5
3.0
3.5
4.0
y_2

Fig. 7a

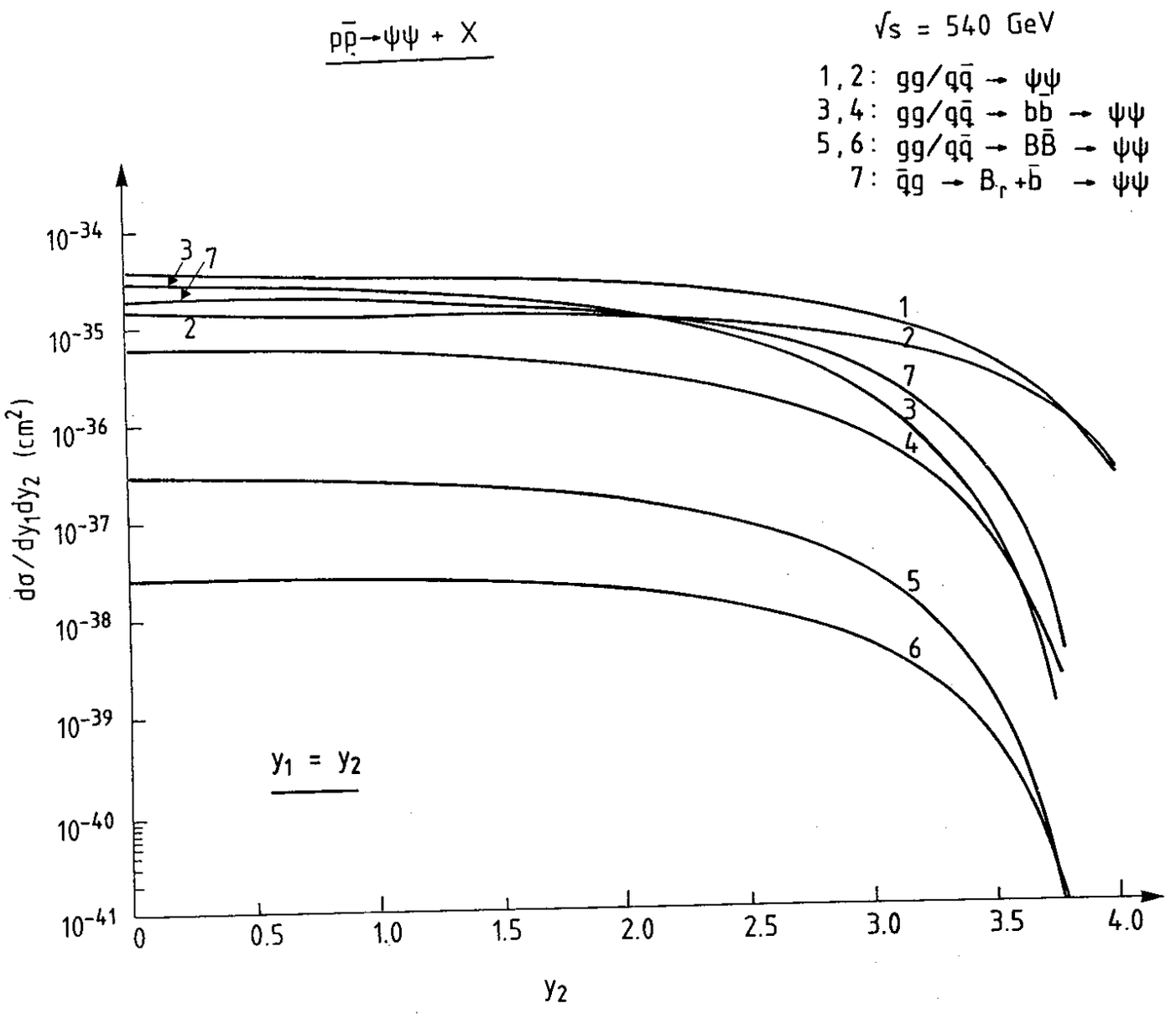
$p\bar{p} \to \psi\psi + X$
$\sqrt{s}$ = 540 GeV
1, 2: $gg/q\bar{q} \to \psi\psi$
3, 4: $gg/q\bar{q} \to b\bar{b} \to \psi\psi$
5, 6: $gg/q\bar{q} \to B\bar{B} \to \psi\psi$
7: $\bar{q}g \to B_r + \bar{b} \to \psi\psi$
$d\sigma/dy_1dy_2$ (cm^2)
10^{-34}
10^{-35}
10^{-36}
10^{-37}
10^{-38}
10^{-39}
10^{-40}
10^{-41}
$y_1 = y_2$
0
0.5
1.0
1.5
2.0
2.5
3.0
3.5
4.0
y_2

Fig. 7b

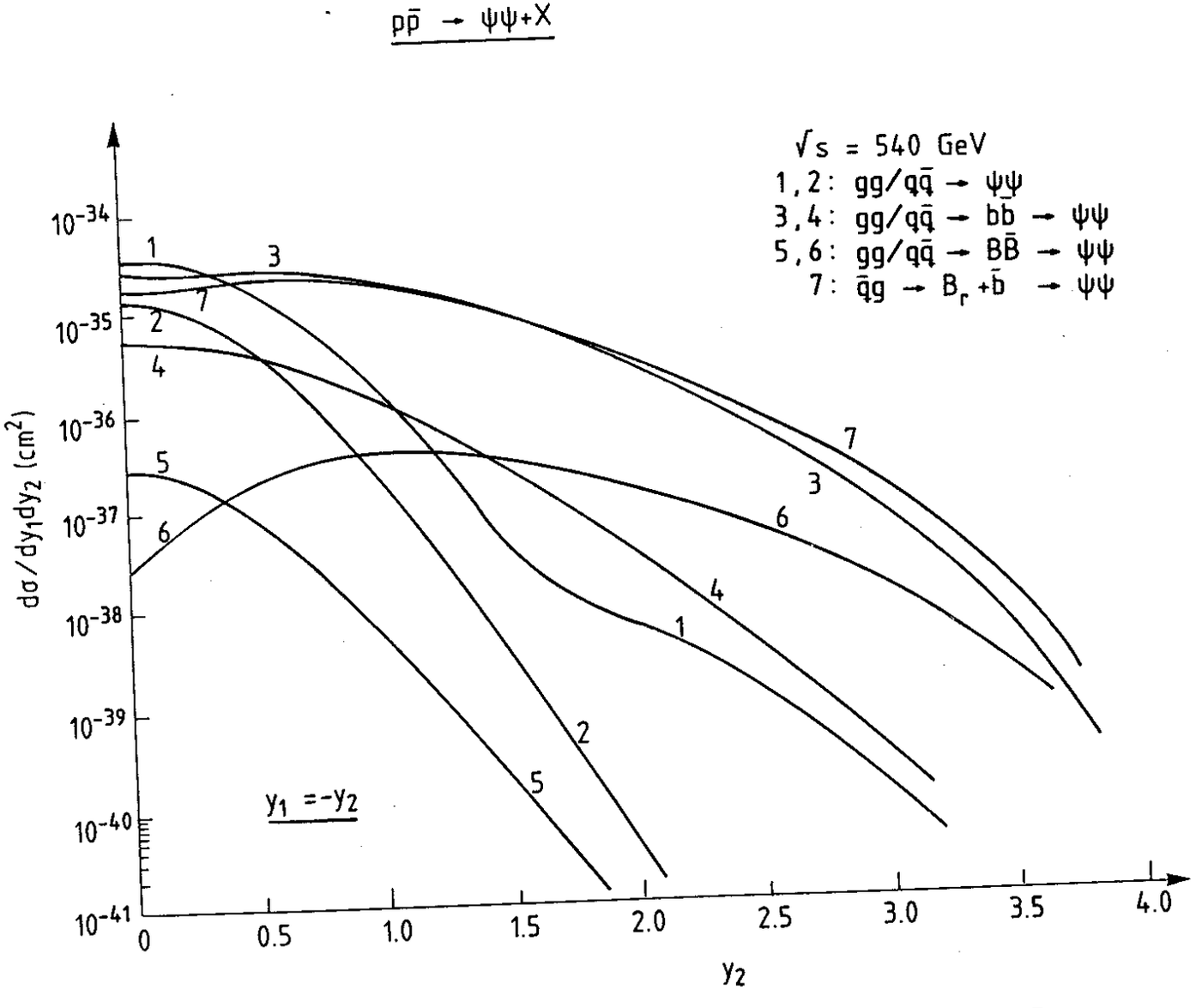
$p\bar{p} \rightarrow \psi\psi + X$
$\sqrt{s}$ = 540 GeV
1, 2: $gg/q\bar{q} \rightarrow \psi\psi$
3, 4: $gg/q\bar{q} \rightarrow b\bar{b} \rightarrow \psi\psi$
5, 6: $gg/q\bar{q} \rightarrow B\bar{B} \rightarrow \psi\psi$
7: $\bar{q}g \rightarrow B_r + \bar{b} \rightarrow \psi\psi$
$d\sigma/dy_1dy_2$ (cm^2)
10^{-34}
10^{-35}
10^{-36}
10^{-37}
10^{-38}
10^{-39}
10^{-40}
10^{-41}
$y_1 = -y_2$
0
0.5
1.0
1.5
2.0
2.5
3.0
3.5
4.0
y_2

Fig. 7c

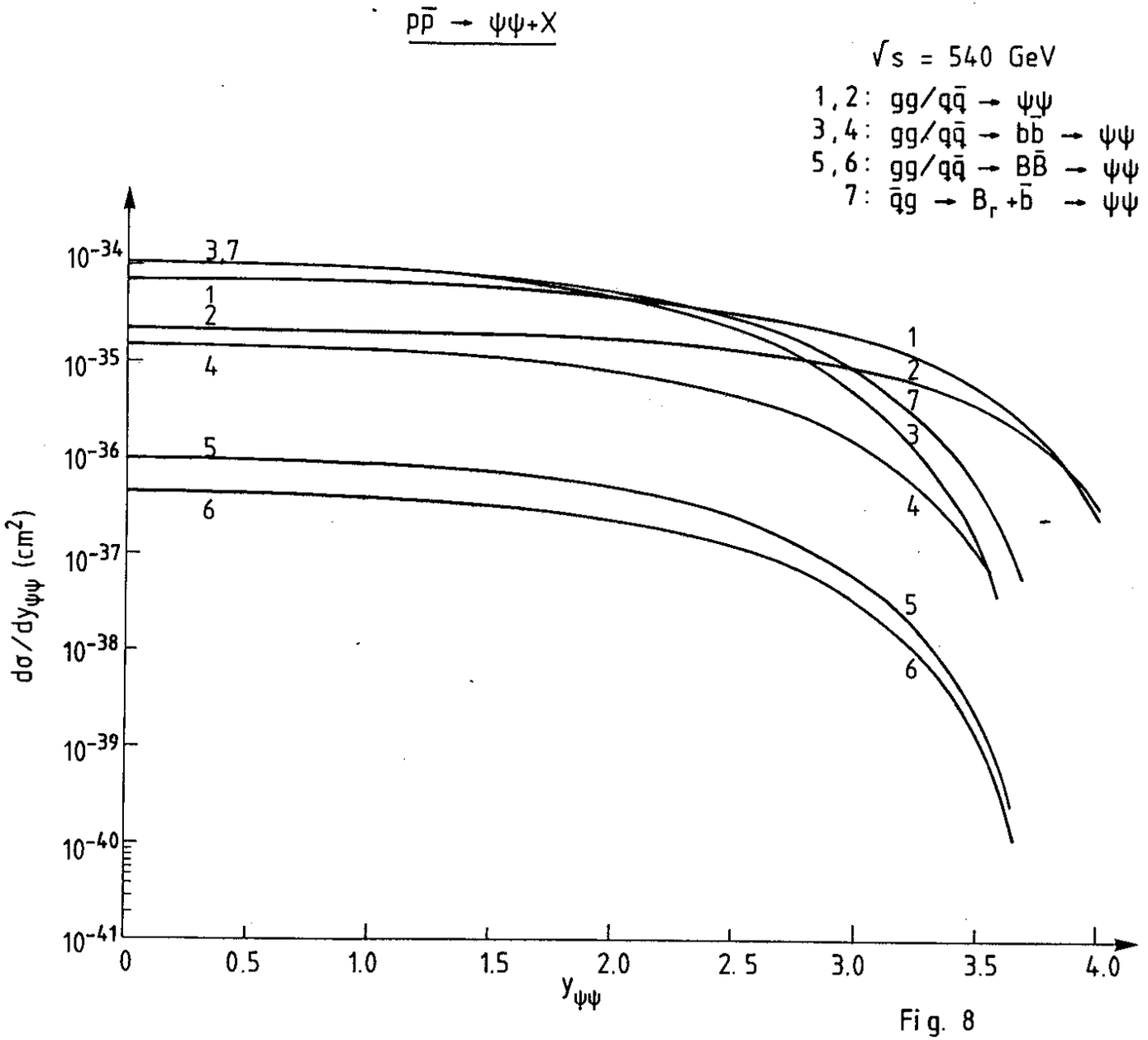
$p\bar{p} \rightarrow \psi\psi + X$
$\sqrt{s}$ = 540 GeV
1, 2: $gg/q\bar{q} \rightarrow \psi\psi$
3, 4: $gg/q\bar{q} \rightarrow b\bar{b} \rightarrow \psi\psi$
5, 6: $gg/q\bar{q} \rightarrow B\bar{B} \rightarrow \psi\psi$
7: $\bar{q}g \rightarrow B_r + \bar{b} \rightarrow \psi\psi$
$d\sigma/dy_{\psi\psi}$ (cm^2)
10^{-34}
10^{-35}
10^{-36}
10^{-37}
10^{-38}
10^{-39}
10^{-40}
10^{-41}
0
0.5
1.0
1.5
2.0
2.5
3.0
3.5
4.0
$y_{\psi\psi}$
3,7
1
2
4
5
6
1
2
7
3
4
5
6

Fig. 8

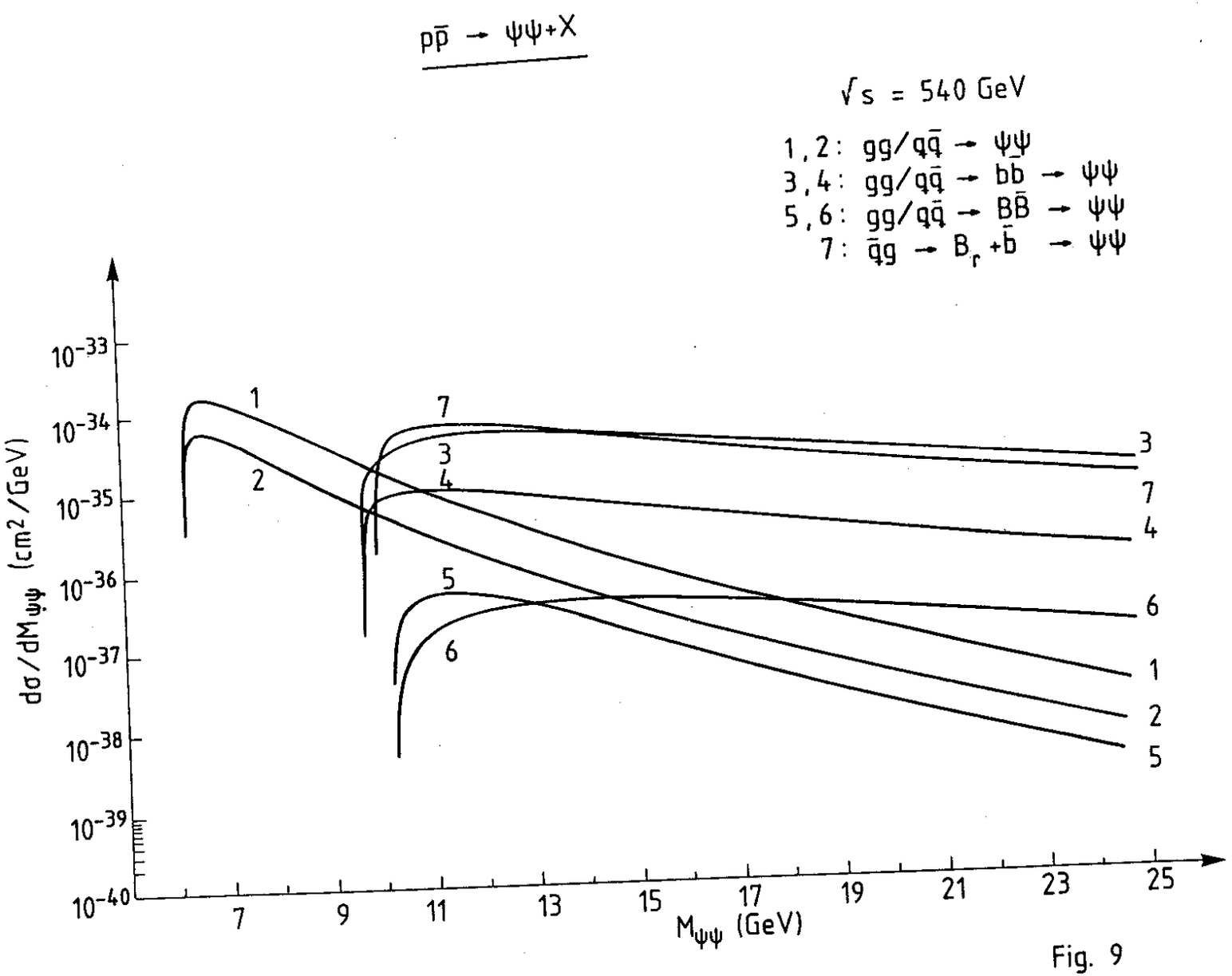
$p\bar{p} \rightarrow \psi\psi + X$
$\sqrt{s}$ = 540 GeV
1, 2: $gg/q\bar{q} \rightarrow \psi\psi$
3, 4: $gg/q\bar{q} \rightarrow b\bar{b} \rightarrow \psi\psi$
5, 6: $gg/q\bar{q} \rightarrow B\bar{B} \rightarrow \psi\psi$
7: $\bar{q}g \rightarrow B_r + \bar{b} \rightarrow \psi\psi$
$d\sigma/dM_{\psi\psi}$ (cm²/GeV)
10^{-33}
10^{-34}
10^{-35}
10^{-36}
10^{-37}
10^{-38}
10^{-39}
10^{-40}
7
9
11
13
15
17
19
21
23
25
$M_{\psi\psi}$ (GeV)

Fig. 9

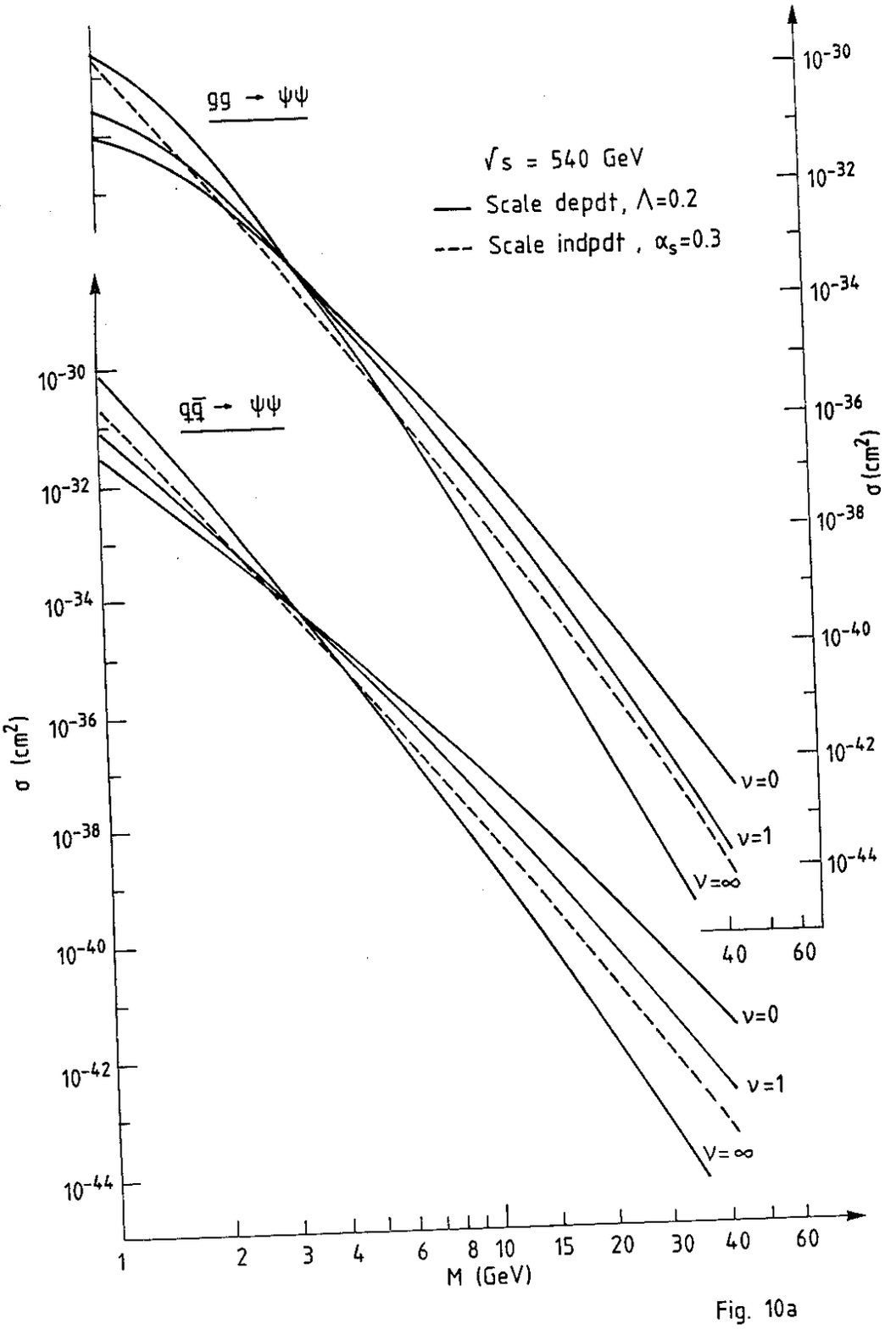
gg → ψψ
√s = 540 GeV
Scale depdt, Λ=0.2
Scale indpdt , αs=0.3
qq̄ → ψψ
ν=0
ν=1
ν=∞
σ (cm²)
M (GeV)
1
2
3
4
6
8
10
15
20
30
40
60
10⁻³⁰
10⁻³²
10⁻³⁴
10⁻³⁶
10⁻³⁸
10⁻⁴⁰
10⁻⁴²
10⁻⁴⁴

Fig. 10a

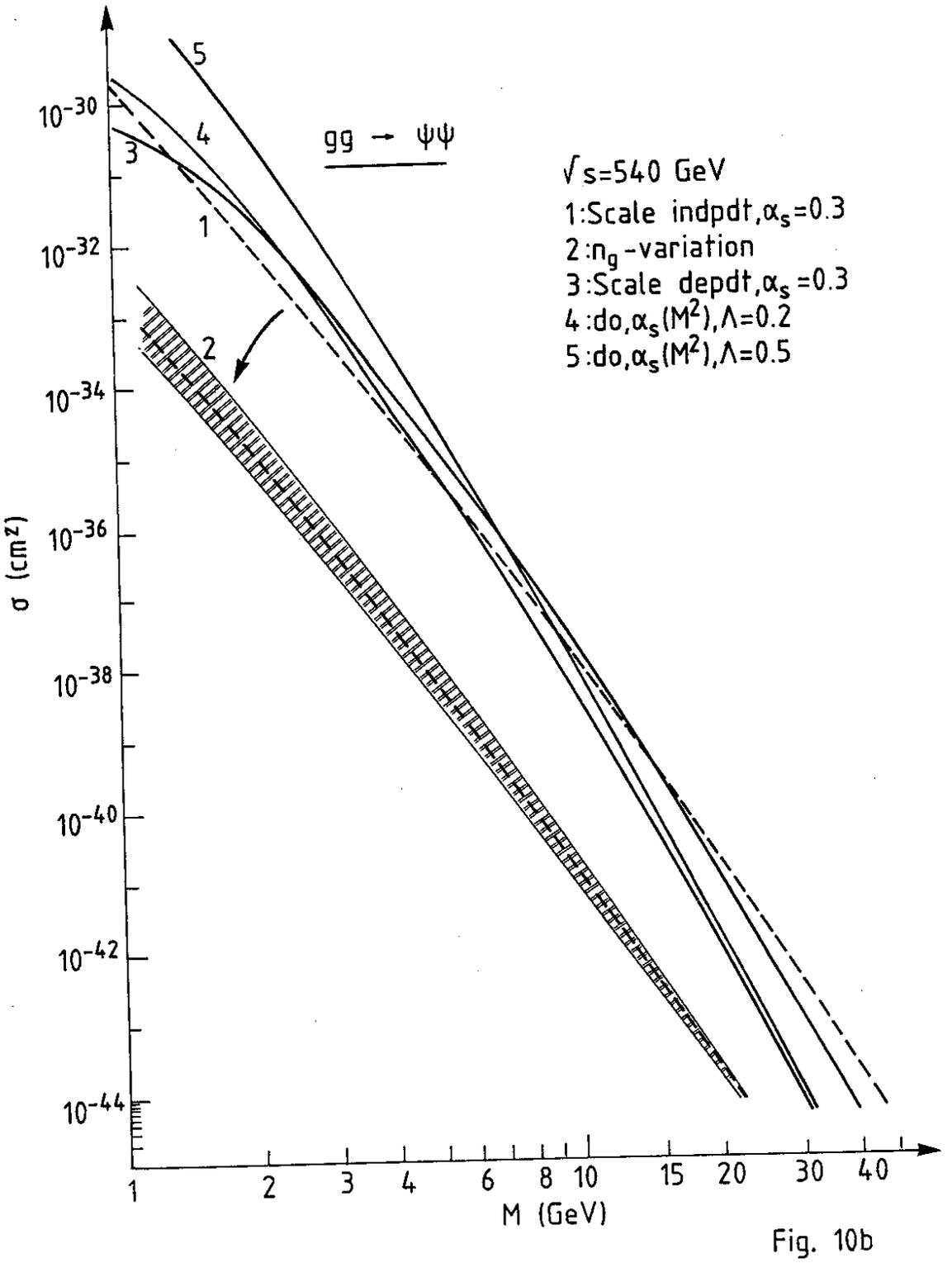
gg → ψψ
√s=540 GeV
1:Scale indpdt,α_s=0.3
2:n_g-variation
3:Scale depdt,α_s=0.3
4:do,$\alpha_s(M^2)$,Λ=0.2
5:do,$\alpha_s(M^2)$,Λ=0.5
σ (cm²)
M (GeV)
10⁻³⁰
10⁻³²
10⁻³⁴
10⁻³⁶
10⁻³⁸
10⁻⁴⁰
10⁻⁴²
10⁻⁴⁴
1
2
3
4
6
8
10
15
20
30
40

Fig. 10b

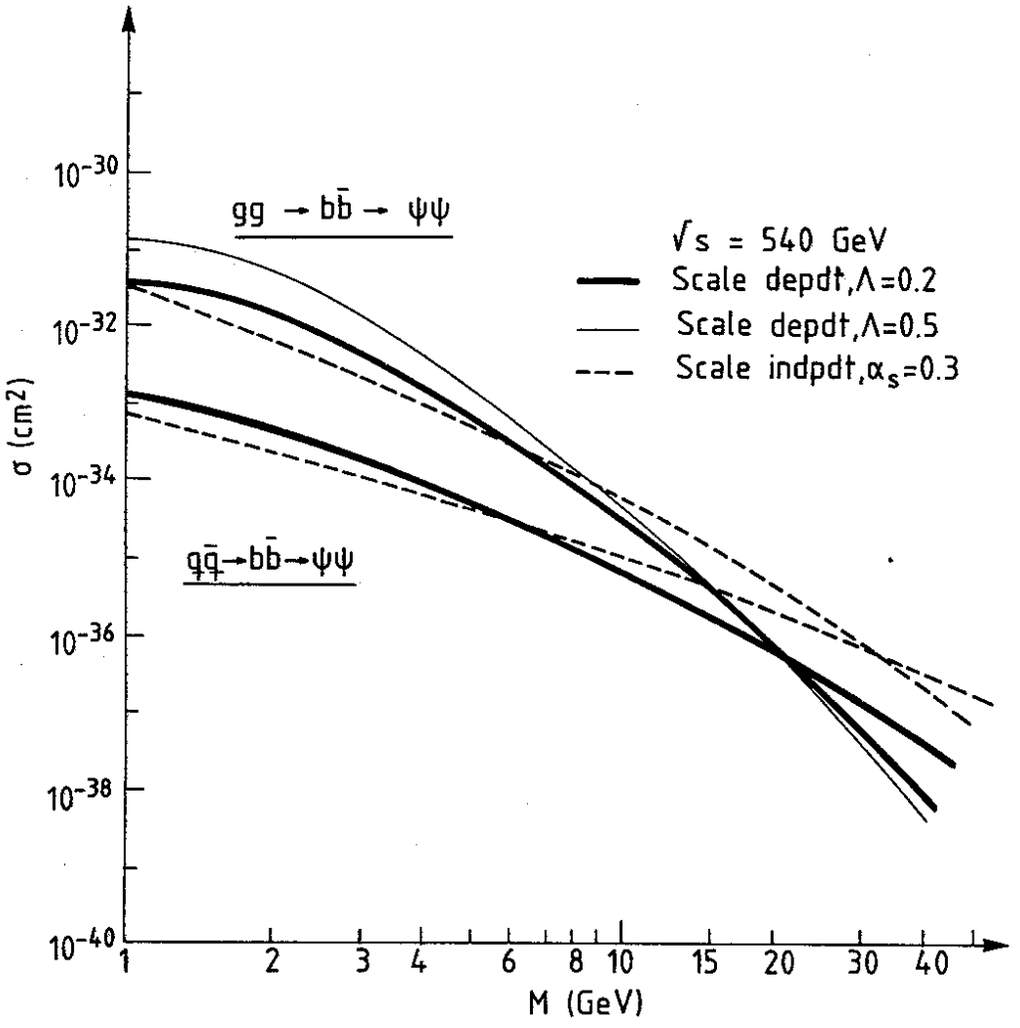
10^{-30}
10^{-32}
10^{-34}
10^{-36}
10^{-38}
10^{-40}
σ (cm²)
gg → bb̄ → ψψ
qq̄ → bb̄ → ψψ
√s = 540 GeV
Scale depdt, Λ=0.2
Scale depdt, Λ=0.5
Scale indpdt, α_s=0.3
1
2
3
4
6
8
10
15
20
30
40
M (GeV)

Fig. 11

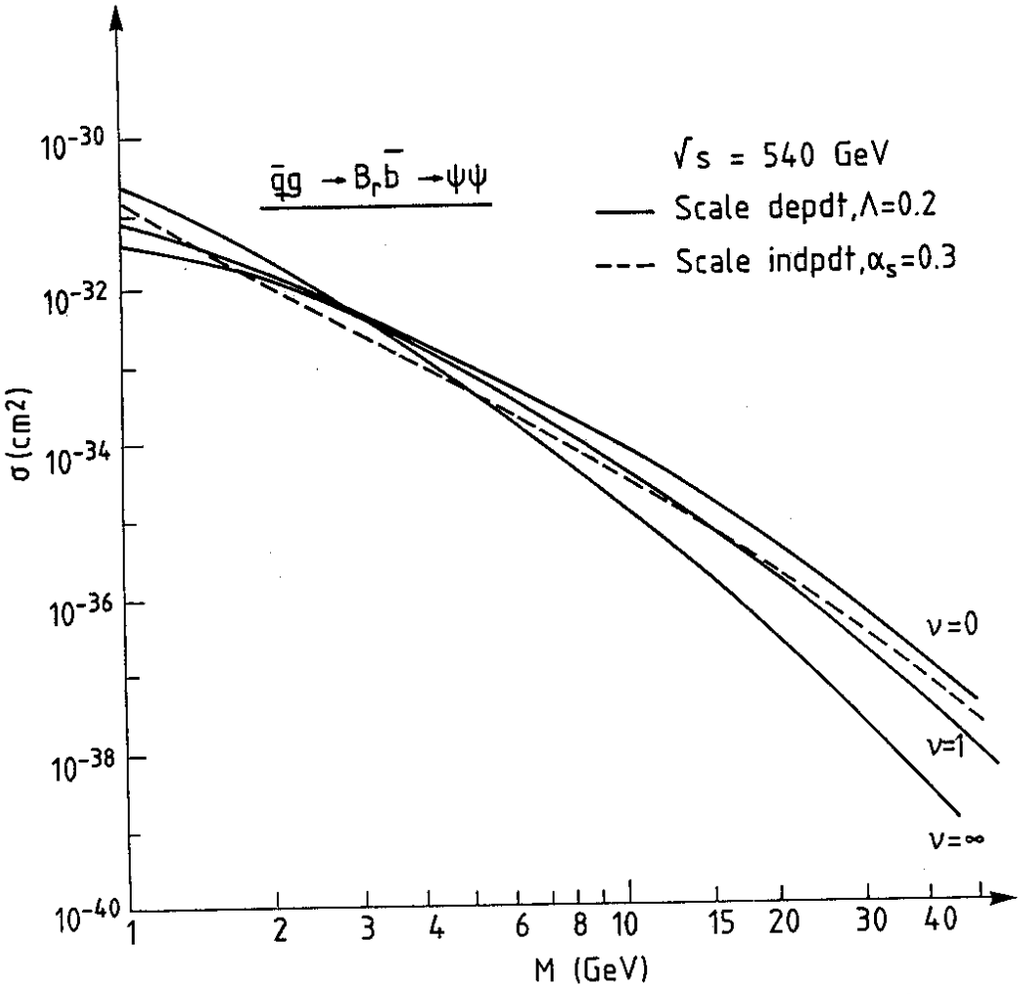
$\bar{q}g \to B_r\bar{b} \to \psi\psi$
$\sqrt{s}$ = 540 GeV
Scale depdt, Λ=0.2
Scale indpdt, α_s=0.3
σ (cm^2)
10^{-30}
10^{-32}
10^{-34}
10^{-36}
10^{-38}
10^{-40}
ν=0
ν=1
ν=∞
1
2
3
4
6
8
10
15
20
30
40
M (GeV)

Fig. 12